



Electron trapping energy states of TiO₂–WO₃ composites and their influence on photocatalytic degradation of bisphenol A



Gregor Žerjav^{a,*}, Muhammad Shahid Arshad^a, Petar Djinović^a, Janez Zavašnik^b, Albin Pintar^a

^a Department for Environmental Sciences and Engineering, National Institute of Chemistry, Hajdrihova 19, SI-1001 Ljubljana, Slovenia

^b Centre for Electron Microscopy and Microanalysis, Jožef Stefan Institute, Jamova 39, SI-1000 Ljubljana, Slovenia

ARTICLE INFO

Article history:

Received 23 December 2016

Received in revised form 15 February 2017

Accepted 17 February 2017

Available online 24 February 2017

Keywords:

TiO₂ nanorods

TiO₂–WO₃ composites

Electron–hole separation

Shallow trapping

Deep trapping

ABSTRACT

Impregnation method was used to synthesize TiO₂–WO₃ composites with two different TiO₂ morphologies (nanorods (R-TiO₂–WO₃) and polyhedral nanoparticles (P-TiO₂–WO₃)). Their structural, morphological, surface properties and electron trapping states were analyzed and correlated to performance in photocatalytic bisphenol A oxidation. TiO₂ nanorods were prepared with alkaline hydrothermal digestion of commercially available high surface TiO₂ nanopowder (DT-51), which was used as a reference for TiO₂ nanoparticles. TEM analysis showed that in R-TiO₂–WO₃ composites WO₃ is dispersed over the surface of TiO₂ nanorods in amorphous form and with increasing amount of WO₃ the TiO₂ crystal structure deteriorates. However, in the case of P-TiO₂–WO₃ composite, multiphase system with monoclinic WO₃ intermixed with anatase TiO₂ was observed. Moreover, P-TiO₂–WO₃ composite showed strong surface acidic sites, which were absent in R-TiO₂–WO₃ composites; this information is significant to understand the depth of the electron trapping states. UV light-induced electron–hole pair excitations and decay dynamics in both TiO₂–WO₃ composites were studied by infrared spectroscopy measurements and information about the conduction band (CB) electrons and surface trapping states of the composites were collected. In the case of composites with high density of shallow trapping states, enhanced photocatalytic activity was observed. On the contrary, lower photocatalytic activity of solids was observed in cases where deep trapping (TiO₂ nanoparticles) or fast recombination (R-TiO₂–WO₃ composite) prevailed.

© 2017 Elsevier B.V. All rights reserved.

1. Introduction

Photocatalysis is a promising technology for water purification, namely catalytic destruction of persistent organic pollutants, such as bisphenol A (BPA), which possesses endocrine disrupting properties and finds widespread use in production of polycarbonates, numerous plastic articles, personal care products, packing materials *etc.* [1]. The main goal of a photocatalyst is to generate hydroxyl radicals, which then react with liquid-dissolved organic pollutants and disintegrate them to H₂O and CO₂ [2]. TiO₂ has been extensively studied and identified as the best photocatalyst for the decomposition of many organic pollutants present in aqueous medium [3] due to its high photocatalytic activity, chemical stability, low cost and nontoxicity [4]. The drawbacks of TiO₂ are: (i) wide band gap energy of 3.2 eV, meaning it can be excited only by ultraviolet (UV) light ($\lambda < 387$ nm); and (ii) fast electron–hole recombination. Effective approaches to resolve these drawbacks are modifications of TiO₂, such as doping with other metal and non-metal elements or coupling with other semiconductors such as Fe₂O₃, CdS, ZnO, Cu₂O and Bi₂O₃ [5–9]. Coupling of TiO₂ with WO₃ to form a heterojunction which improves the charge separation by trapping the photo-generated electrons and extending the energy range of photoexcitation toward the visible range, seems to be an efficient way to improve the photocatalytic performance of TiO₂ [10–12]. WO₃ is an inexpensive n-type semiconductor, low in toxicity as well as stable in acidic and oxidative conditions with relatively small band gap (2.6 eV) [13]. There are many methods available for the synthesis of TiO₂–WO₃ composites, such as sol–gel [14], ball milling [15], multiple grafting [16], incipient wetness impregnation [17], flame spray synthesis [18] *etc.*

In the semiconductor photocatalysis, an electron (e[−]) in the valence band (VB) is excited to the conduction band (CB) by a photon with energy equal or greater than the band gap energy. The holes (in VB) and electrons (in CB) can either: (i) reduce and oxidize substrates adsorbed on the photocatalyst's surface, or (ii) recombine with each other without any chemical reaction. When

* Corresponding author.

E-mail address: gregor.zerjav@ki.si (G. Žerjav).

the activity of a catalyst is lower than expected, this is generally attributed to fast recombination at unknown “recombination sites”, and when the activity is higher the recombination is suppressed by some means [19]. Thus, “recombination” has been used as a convenient term for explanation of photocatalytic activity without its in depth understanding [19].

TiO₂ turns black or blue-black when heated in reducing atmosphere due to the release of oxygen and formation of Ti³⁺ [19]. This phenomenon results in the formation of electron-filled donor levels located below the CB of the n-type TiO₂, called electron traps (ETs) [19]. These electron traps accept excited electrons; if energy difference between the CB bottom and ETs is smaller than the thermal energy of the electrons, the electrons in these *shallow traps* can be thermally excited to CB and can participate in the redox reactions. Thus, occupied shallow electron trapping states are considered necessary for the reduction of oxygen at the TiO₂ surface [20,21]. On the other hand, migration of electrons between CB and ETs might not be possible if the depth of traps is much larger (above 0.15 eV) than thermal energy (0.026 eV at 29 °C). In this case, electrons trapped by these *deep traps* cannot be excited thermally to the CB and eventually recombine with holes (h⁺). Consequently, enhancement of photocatalytic activity is supported by the large density of shallow trapping sites, whereas presence of deep traps is expected to reduce the photocatalytic activity [19,22].

Jiang et al. reports in his work, that doping TiO₂ with NO_x species can lead to formation of midgap states, just above the top of TiO₂ VB and that V_O lead to formation of midgaps states which is energetically under CB of TiO₂ and comprising the 3d state of Ti⁴⁺ ions. The synergistic result was narrowing of the bandgap of TiO₂ [23]. Despite the fundamental importance of these electron trapping energy states, little is known about them. Thus, it is of high importance to study the physical nature and function of these surface trapping sites. *In situ* and *operando* observation of electron–hole recombination and trapping states in photocatalysis is a very challenging task difficult, because recombination generally proceeds with the release of heat which is not easy to detect [24]. Bowman et al. used pump-probe spectroscopy for detection of electron–hole recombination of heterogeneous photocatalytic reactions [25]. Trapping and recombination of the photo-generated charge carriers have been studied with UV/Vis spectroscopy [26] and electron paramagnetic resonance [27]. However, infrared (IR) spectroscopy can reveal in-depth information about the transfer of electrons to CB and surface energy states, which trap photo-generated electrons. It is generally believed that conventional IR spectroscopy gives limited information about electronic processes occurring on the surface of TiO₂ because: (i) the timeframe of electronic processes (femto to milliseconds) is considerably shorter than the time of IR spectrum acquisition (seconds to minutes), and (ii) lack of specific interaction of electrons and holes with IR irradiation. Indeed, the injection of electrons into the CB and concomitantly the generation of holes in the VB occur in femtoseconds, but the trapping processes of electrons and holes can be observed on the time scale of seconds to minutes [28]. The timeframe of electronic processes strongly depends on the medium in which the solid is embedded and can vary by 13 orders of magnitude. Also, cryogenic temperatures can significantly increase life-span of charge carriers [25,29,30]. Kukimoto et al. probed doped ZnS samples in 1960s under UV-light irradiation and observed a broad IR absorption peak at around 0.12 eV (968 cm^{−1}), which was attributed to electron excitation from hydrogenic donor centers (*shallow trapping states*) to the CB [31–33].

The aim of this study was to synthesize and investigate the properties of TiO₂–WO₃ composites, which are based on morphologically very different TiO₂ substrates, namely TiO₂ polyhedral nanoparticles (P-TiO₂–WO₃) and TiO₂ nanorods (R-TiO₂–WO₃), which were prepared by means of a hydrothermal procedure.

For both TiO₂ morphologies, we investigated how the increasing amount of WO₃ influences the structural and electronic properties of the composites, and how this manifests itself in the photocatalytic activity toward liquid-phase BPA degradation.

2. Experimental

2.1. Catalyst preparation

Titanate nanorods (TiO₂ NRs) were prepared using an alkaline hydrothermal synthesis, which is similar to the procedure reported by Kasuga et al. [34]. First, 2 g of TiO₂ nanoparticles (DT-51, provided by Crystal company) was dispersed in 150 ml of 10 M aqueous NaOH solution by means of ultrasonic homogenizer. The solution was then poured into a 200 ml Teflon-line autoclave and heated at 130 °C for 24 h. The obtained white precipitate was separated from the reaction solution by centrifugation and the wet cake was washed with deionized water in order to neutralize the product. The obtained sodium titanate was further treated with 0.1 M HCl solution to exchange Na⁺ with H⁺. After protonation, titanates were thoroughly washed with deionized water and finally dried in vacuum under cryogenic conditions.

TiO₂–WO₃ composites were prepared by means of impregnation method using 1 g of TiO₂ nanoparticles (DT-51, provided by Crystal company) or TiO₂ NRs and 5 ml of aqueous solution of ammonium meta tungstate hydrate (AMT, (NH₄)₆H₂W₁₂O₄₀·xH₂O, Sigma–Aldrich). The AMT–TiO₂ suspension was stirred for 2 h at room temperature. The slurry was dried overnight and calcined at 500 °C in air for 2 h. The control materials: polyhedral TiO₂ nanoparticles (P-500), TiO₂ NRs (R-500) and pure WO₃ (WO₃–500) were subjected to identical thermal treatment. The TiO₂–WO₃ composites having nominal loadings of W in the range of 0–6.4 wt.% were prepared (for example, abbreviation R+4.40 marks a R-TiO₂–WO₃ composite with a nominal W loading of 4.40 wt.%).

2.2. Catalyst characterization

Microstructure and chemical composition of the composites were studied using a 200 kV transmission electron microscope (TEM; JEM-2100, Jeol Inc.) equipped with LaB6 filament and energy dispersive X-ray (EDS) spectrometer (EX-24063JGT, Jeol Inc.). For TEM analysis, the samples were dispersed in absolute ethanol, sonicated, and a drop of ethanol containing the sample was placed on TEM Cu grid and vacuum-dried for 24 h before inserted them into the TEM. The micrographs were recorded with a high-resolution slow-scan CCD camera (Orios DC1000, Gatan Inc.). The crystal structure data for the simulation of the selected area diffraction pattern (SAED) patterns were obtained from literature [35].

For the atomic force microscope (AFM) measurements, a drop of suspension solution of the R+4.40 sample was placed on a clean Si wafer and dried overnight before the AFM measurements. The AFM measurements were performed using Agilent 5500 AFM in the tapping mode with a cantilever from Nanosensors (PPP-NCH-10).

X-ray powder diffraction patterns of the catalysts were collected on PANalytical X'pert PRO MPD diffractometer with Cu Kα1 radiation (1.54056 Å) in reflection geometry in the range of 20–90° in steps of 0.034°. PDF standards from the International Centre for Diffraction Data (ICDD) were used for the identification of crystalline phases.

UV/Vis diffuse reflectance (DR) spectra were obtained at room temperature using Perkin–Elmer Lambda 35 UV-Vis spectrophotometer equipped with the RSA-PE-19M Praying Mantis accessory. The background correction in the range of 200–900 nm was recorded using white reflectance standard Spectralon®.

Acidic properties of synthesized composites were analyzed by temperature programmed desorption of pyridine (Py-TPD) using Pyris 1 TGA instrument (Perkin–Elmer). Samples were heated up to 500 °C at 10 °C/min and held at this temperature for 10 min. Then they were cooled to 120 °C and saturated with a N₂–pyridine stream until constant mass. Excess of pyridine was removed with a flow of pure N₂. Py-TPD analysis was carried out by heating the samples up to 800 °C at rate 20 °C/min.

In situ UV light diffuse reflectance IR spectroscopy (DRIFT) spectra of the TiO₂–WO₃ composites were recorded using a Frontier analyzer (Perkin–Elmer) equipped with a MCT detector and DiffusIR™ cell from Pike Scientific. Spectral resolution of 4 cm^{−1} was employed and 32 scans were accumulated between 450 and 4000 cm^{−1}. Experiments were carried out under continuous Ar flow of 25 ml/min and constant sample temperature of −140 °C, which was maintained using LN₂. A light emitting diode (LED) with peak output at 365 nm (FWHM ~16 nm) (Prizmatix, model FC3-LED) was used as a light source with irradiation power of 100 mW. The wavelength of the LED light source was chosen in order to resemble the high pressure Hg lamp, which has a maximum emission peak at 365 nm and was used in BPA degradation experiments. The samples were irradiation with UV-light for 28 mins (light ON) and then light was turned off to observe the electronic decay kinetics (light OFF). Spectra were collected and processed using Spectrum software (Perkin–Elmer, v10.03.02) and for time-resolved FTIR measurements Spectrum Timebase software (Perkin–Elmer, v3.1.2) was utilized. The excitation-decay kinetic data were obtained from time-resolved FTIR measurements with temporal resolution of around 4 s. The measured absorbance intensity has an uncertainty of about ±0.0001 a.u.

Elemental analysis of fresh and spent TiO₂–WO₃ composites performed with a CHNS analyzer (Perkin–Elmer, model 2400 Series II) was employed to evaluate the amount of carbon accumulated on the catalyst surface during photocatalytic oxidation runs.

2.3. Photocatalytic oxidation experiments

For the photolytic/photocatalytic experiments a solution of 10 mg/l BPA in ultrapure water (18.2 MΩ cm) was used. The experiments were performed in a 250 ml batch slurry reactor at atmospheric pressure, which was magnetically stirred (600 rpm) and thermostated at 20 °C (Julabo, model F25/ME). Solution was purged with purified air during the whole experiment (45 l/h). The catalyst concentration used in the experiments was 62.5 mg/l. Ultrasonication was employed to suspend the catalyst before adding to the BPA solution. Illumination of the suspension with UVA Hg lamp (150 W, maximum at λ = 365 nm) started after 30 min where the suspension was kept in dark (“dark” period) for the establishing of equilibrium of the sorption process. The Hg lamp was positioned in a water-cooling jacket which was immersed vertically in the center of the batch slurry reactor.

2.4. Analysis of end-product solutions

During the experiment, 1.5 ml samples were continuously withdrawn, filtered through 0.2 μm membrane filter and analyzed with HPLC (Thermo Scientific, model Spectra) to determine temporal BPA conversions; details about the analytical protocol can be found elsewhere [36]. The level of mineralization, i.e. the total amount of removed organic substances in aqueous-phase samples withdrawn at the end of the photolytic/photocatalytic experiment (25 ml), was determined by measuring the total organic carbon (TOC) content. TOC measurements were carried out with an advanced TOC analyzer (Teledyne Tekmar, model Torch) equipped with a high pressure NDIR detector.

3. Results and discussion

3.1. Catalyst characterization

Fig. 1a shows TEM image of P-500 sample. Nanoparticles have an ellipsoid shape with a diameter of around 20 nm and length of around 30 nm. The nanoparticles are well crystalline with random crystallographic orientations as shown in the dark-field TEM (DF-TEM) image in Fig. 1b. Furthermore, in the high-resolution TEM (HR-TEM) image (Fig. 1c), one can see individual nanoparticles are anatase crystallites as shown by the fringes with preferential crystallographic orientation along [101] direction. The SAED pattern (inset Fig. 1c) compares the experimental and simulated data for anatase and rutile phases and it can be clearly seen that there is only anatase phase present in the investigated sample (Fig. 1c). TEM image presented in Fig. 2a of P+4.40 composite, shows that the general morphology and dimensions of the nanoparticles is similar as in the P-500 sample. However, there are differences in TiO₂ morphology regarding sharp edges present in these composite as shown in Fig. 2b. The TEM-EDS analysis shows that the composite (P+4.40) consists of Ti, W and O as shown in inset of Fig. 2a. The TEM-EDS elemental analysis results for P+4.40 composite are provided in supplementary data (Table S1); measured W content was 3.6 wt.% which is very close to its nominal value of 4.40 wt.%. From the SAED pattern in Fig. 2c we can see that the anatase TiO₂ phase is present, however we have observed additional intensities represented with the arrows. The analysis of the d-values of the additional peaks show that they belong to the monoclinic WO₃ (PDF No. 005-0431), results are presented in supplementary data (Fig. S1). Thus, P+4.40 composite consists of anatase TiO₂ and monoclinic WO₃.

A proper rod-like morphology consisting of anatase crystals with preferable growth along [101] direction was observed in the HR-TEM images of R-500 sample with length around 70 nm and diameter around 10 nm, as shown in Fig. 3a and b. The SAED pattern compared with simulation (Fig. 3c) reveal that the R-500 sample consists of pure anatase phase. The TEM image of R+4.40 sample (Fig. 4a and b) shows a rod-like morphology with the similar diameter and length as for the R-500 sample. In the SAED patterns of R+4.40 (Fig. 4c), no additional peaks were observed besides the anatase phase. Careful analysis of Fig. 4a revealed an amorphous material (~10 nm) encapsulating TiO₂ NRs which might belong to WO₃. Fig. 5a is showing low magnification high angle annular dark field TEM (HAADF-TEM) image indicating most part of the sample (R+4.40) is well crystallized. Scanning TEM-EDS (STEM-EDS) elemental mapping analysis of the R+4.40 sample shows W is present in the composite and uniformly distributed as shown in Fig. 5c. TEM-EDS elemental analysis results for R+4.40 composite are provided in supplementary data (Table S1). Measured W content was 3.9 wt.%, which is very close to its nominal value of 4.40 wt.%. Based on the TEM analysis, the R+4.40 composite consists of anatase TiO₂ NRs covered by an amorphous WO₃ layer.

We can conclude that TiO₂ is present in the anatase form independent of TiO₂ morphology (nanoparticles or nanorods). In case of TiO₂ nanoparticle composites (P+4.40), WO₃ is present in crystalline monoclinic form. In the SAED patterns of the TiO₂ nanorod composite (R+4.40), WO₃ peaks are missing but the STEM-EDS and SEM-EDS mapping (not shown here) clearly showed that W is present in the sample in amorphous form.

In order to obtain a clear indication of the WO₃ on the surface of the R+4.40 composite, AFM images were further acquired. Fig. 6 is showing the AFM image of an individual TiO₂–WO₃ nanorod composite and Fig. 6 inset is representing the line profile (P) taken along the length of the nanorod. From this observation one can clearly see that there is a ~10 nm thick layer on the surface of the TiO₂ nanorod, the dimensions (diameter 10 nm and length 60 nm) are consistent with TEM results (see Fig. 4a and b). Thus, the observed structure

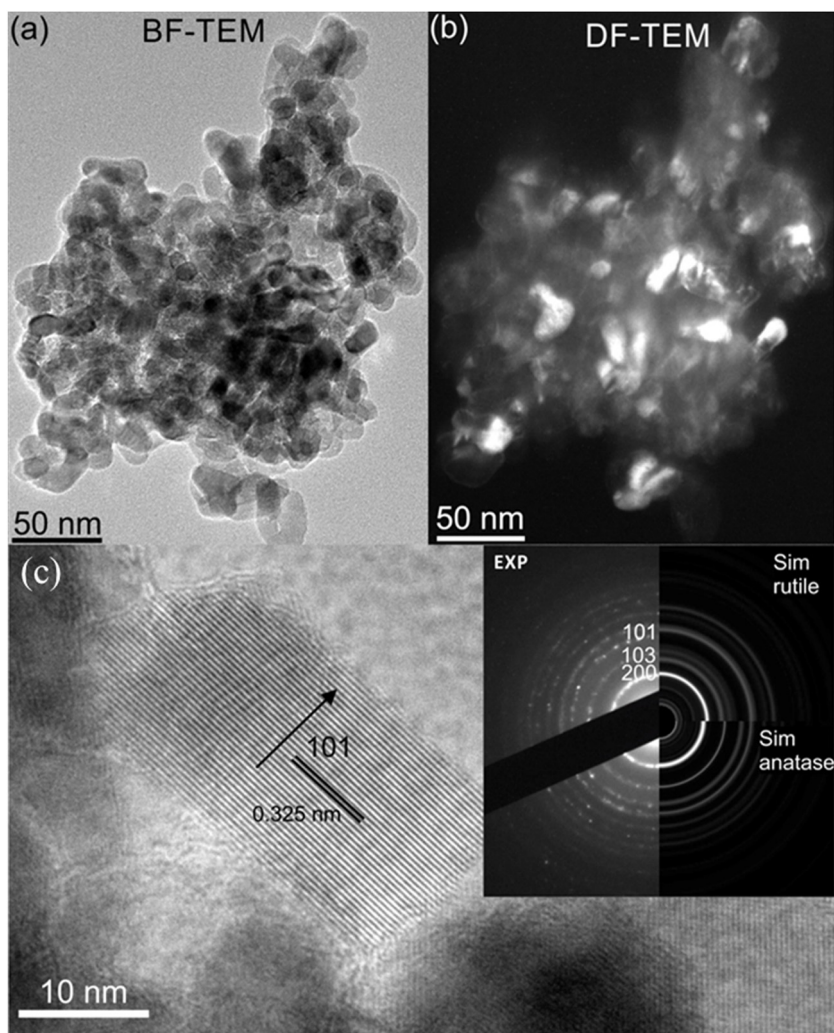


Fig. 1. TEM micrograph of P-500 nanoparticles showing (a) bright field mode (BF-TEM) and (b) dark-field mode (DF-TEM) pair to illustrate random orientation of single-crystal particles of anatase. (c) High resolution TEM image of the individual anatase TiO_2 nanoparticle with preferential crystallographic growth along [101] direction, inset shows experimental selected area electron diffraction (SAED) pattern of P-500 sample compared with simulation patterns of anatase and rutile phase.

in the AFM image is a TiO_2 nanorod which is partly covered with an amorphous WO_3 layer. In a few previous reports on TiO_2 nanorods loaded with WO_3 [37–39], indication was provided that WO_3 forms an amorphous overlayer. However, no AFM images were presented to clarify this point.

Fig. 7 presents XRD diffraction patterns of P- TiO_2 - WO_3 (Fig. 7a) and R- TiO_2 - WO_3 (Fig. 7b) composites with different WO_3 loadings, as well as of pure TiO_2 and WO_3 samples. All the diffraction peaks of composites with various WO_3 loadings match well with the standard data of anatase TiO_2 structure (JCPDS 21-1272). The peaks at 25.4° , 38.0° , 48.2° , 54.0° , 55.2° , 62.9° , 70.5° and 75.3° are attributed to diffractions of (101), (004), (200), (105), (211), (204), (220) and (215) orientations of anatase TiO_2 , respectively. In the case of R- TiO_2 - WO_3 composites (Fig. 7b), the intensity of the (101) diffraction peak at 25.3° decreased with increasing amount of WO_3 in the composite, which indicates either the reduction of crystallinity of the anatase phase, or coverage of anatase TiO_2 with amorphous WO_3 layers as observed in TEM and AFM. However, P- TiO_2 - WO_3 composites based on TiO_2 nanoparticles did not show this behavior. The anatase crystallite sizes, calculated from the corresponding width of the (101) diffraction peak by means of Scherrer formula, are presented in Table 1. We can see that for P- TiO_2 - WO_3 composites there is no significant change in the anatase crystallite size when increasing the amount of WO_3 . However, in the case of R-

Table 1

Average TiO_2 anatase crystallite size of the composites and band gaps for TiO_2 + WO_3 composites evaluated by means of Tauc plot.

Sample	Anatase crystallite size, nm	Unit cell size, nm	Band gap, eV
P-500	20.9	0.378(4)	3.31
P+0.45	20.3	0.378(5)	3.27
P+2.24	20.3	0.378(6)	3.26
P+4.40	20.0	0.378(7)	3.21
R-500	16.3	0.378(4)	3.28
R+0.45	14.9	0.378(5)	3.25
R+2.24	14.4	0.378(5)	3.24
R+4.40	13.2	0.378(5)	3.24
WO_3 -500	/	/	2.64

TiO_2 - WO_3 based composites, the crystallite size decreases with increasing amount of WO_3 . Further, it should be noted that the diffraction peaks of WO_3 cannot be found in XRD patterns of any composite examined (Fig. 7). This is in agreement with the observations of other authors [15,18,39–41]. The possible reason could be that WO_3 crystallite size is too small and below the detection limit of XRD (P- TiO_2 - WO_3), or as an amorphous layer covering TiO_2 (R- TiO_2 - WO_3). The XRD pattern (Fig. 7a) of WO_3 -500 sample exhibits peaks at 23.1° , 24.4° and 31.2° , which are diffractions of (002), (200)

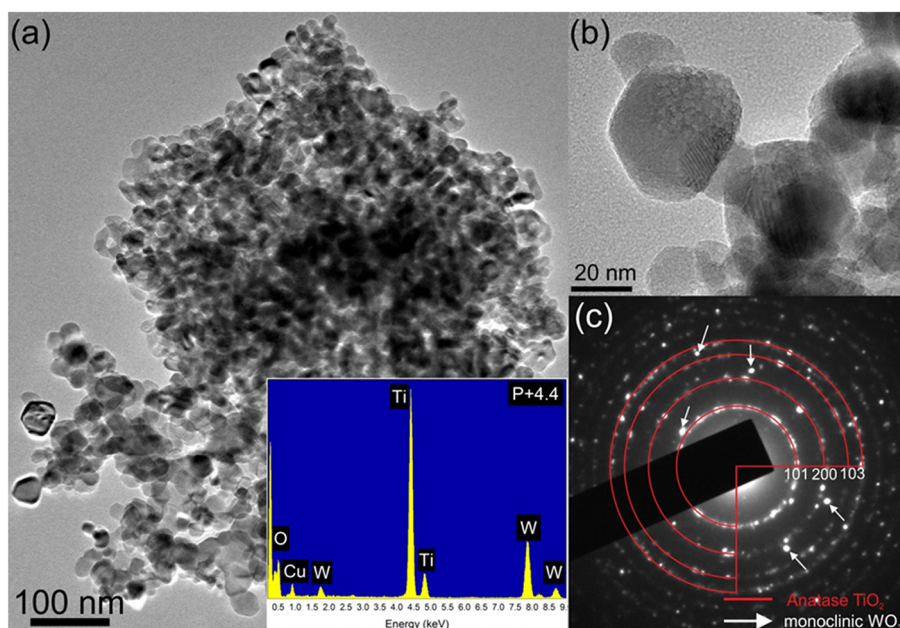


Fig. 2. (a) TEM of P+4.40 composite, inset is showing TEM-EDS analysis on same composite (the Cu signal originates from support grid), (b) high magnification image of the composite showing different morphology, (c) experimental SAED pattern of P+4.40 composite compared with simulated patterns of anatase TiO_2 and monoclinic WO_3 phase.

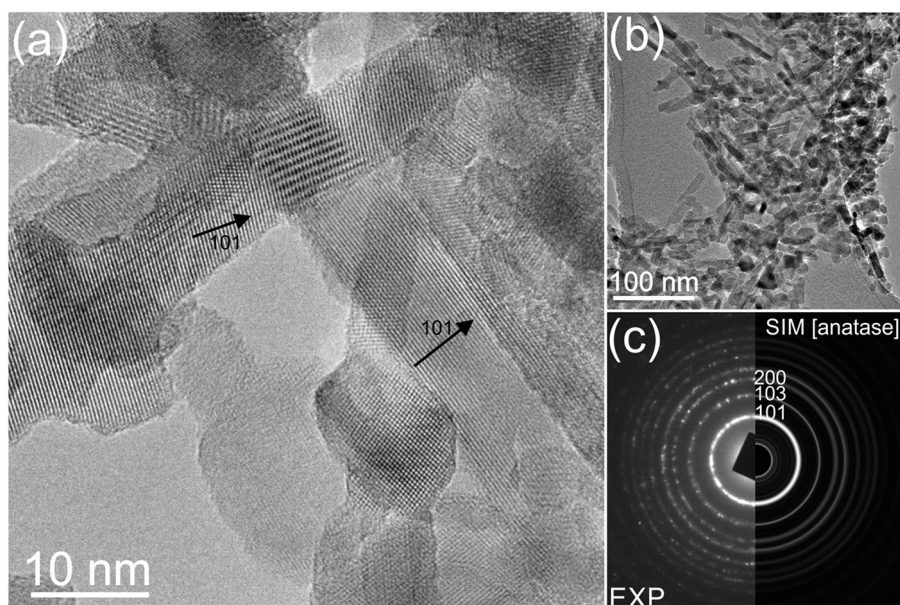


Fig. 3. (a) High resolution transmission electron micrograph (HR-TEM) of anatase nanorods, (b) overview TEM image of the R-500, (c) experimental SAED pattern of R-500 sample compared with simulated patterns of anatase TiO_2 phase.

and (202) orientations of monoclinic WO_3 form (JCPDS 43-1035) [42].

The optical behavior of prepared TiO_2 – WO_3 composites with different WO_3 loadings is presented in Fig. 8a and b for P- TiO_2 – WO_3 and R- TiO_2 – WO_3 composites, respectively. Fig. 8c and d present the Tauc plots obtained from the UV/Vis DR data and in Table 1, the obtained band gap energies are presented. For WO_3 –500 sample we observed a wide range of light absorption with a sharp absorption edge at 470 nm, which corresponds to the band gap (E_g) of 2.64 eV, typical for monoclinic WO_3 [37]. In case of P-500, the band gap energy is 3.28 eV which corresponds to TiO_2 anatase phase. With increasing amount of WO_3 in TiO_2 – WO_3 composites, the absorption edge is incrementally shifted toward higher wavelengths, but the shift is not sufficient to trigger the electron–hole separation of

the catalysts by visible light. Similar results have been reported by other authors [38,43,44], where the modification of TiO_2 with WO_3 was performed using comparable preparation procedures. In case of P- TiO_2 – WO_3 based composites, absorption edge increases from 380 to 395 nm. As a result, in this case, it can be claimed that a broader range of wavelengths can be absorbed and utilized in the catalysis. In the case of R- TiO_2 – WO_3 composites, the WO_3 impact on the capability of the material for absorption of a broader range of wavelengths is negligible. For the R- TiO_2 – WO_3 composites, the absorption edge at around 390 nm was measured. Basnet et al. [45] reports in his work that the absorption edge of amorphous WO_3 is 390 nm which is an additional clue that amorphous WO_3 is present in the R- TiO_2 – WO_3 composites. This is in line with results of TEM, AFM and XRD analyses.

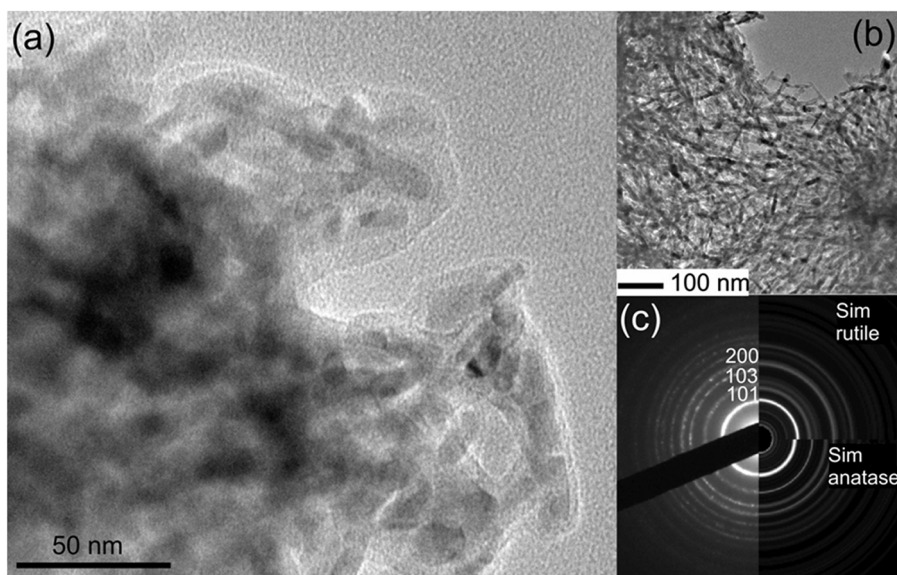


Fig. 4. (a) HR-TEM of R+4.40 composite showing an amorphous layer covering the nanorods, (b) low magnification TEM image of the R+4.40, (c) is showing experimental SAED pattern of R+4.40 composite compared with simulated patterns of anatase and rutile TiO_2 phases.

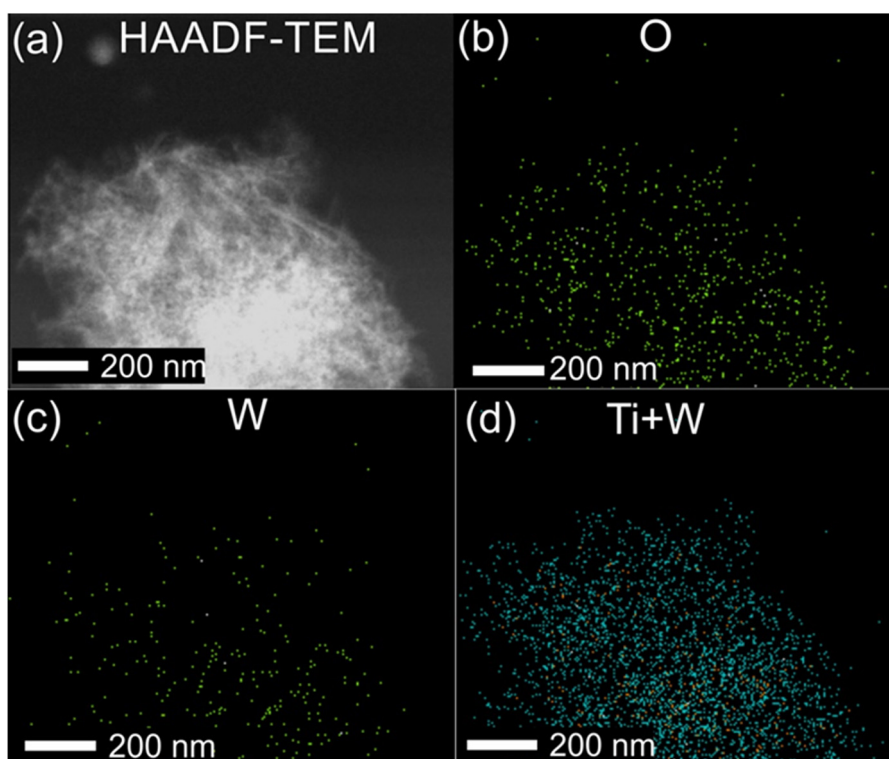


Fig. 5. (a) HAADF-TEM image of the R+4.40 composite. STEM-EDS elemental mapping of R+4.40 composite for (b) Oxygen map (c) Tungsten map and (d) Overlay of titanium and tungsten maps.

Table 2

Density and quantity of acidic sites determined with Py-TPD for P- TiO_2 - WO_3 and R- TiO_2 - WO_3 composites with 4.40 wt.% W loading.

Catalyst	Density of acid sites, mmol/m^2	Quantity of acid sites, mmol/g	Pyridine desorption T, $^{\circ}\text{C}$
P-500	0.0025	0.175	280, 380, 550
P+4.40	0.0023	0.185	280, 380, 525
R-500	0.0026	0.276	280
R+4.40	0.0022	0.324	280

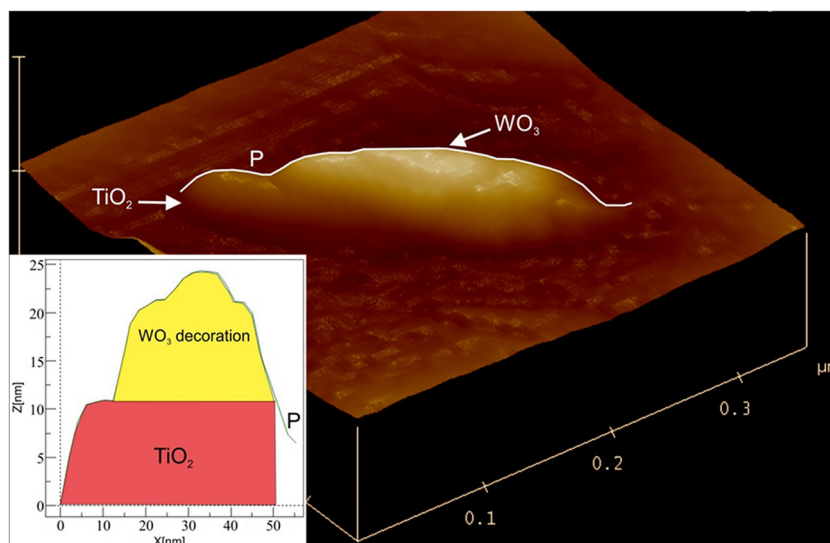


Fig. 6. Height image of the R+4.40 composite sample. The inset shows line profile taken along the length of the nanorod, schematic is representing how WO_3 decorates the surface of TiO_2 nanorod.

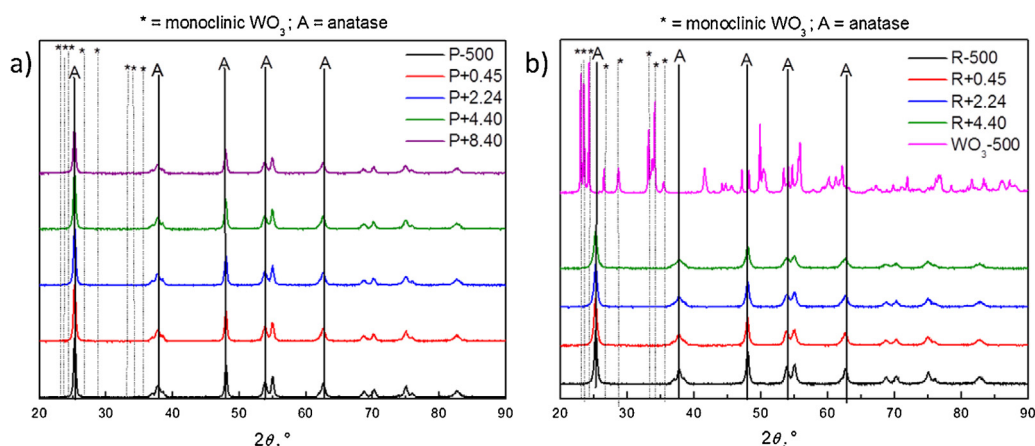


Fig. 7. X-ray diffraction patterns of (a) P- TiO_2 - WO_3 and (b) R- TiO_2 - WO_3 composites with different WO_3 loadings. Diffractograms of P-500, R-500 and WO_3 -500 samples are shown for comparison.

Pyridine-TPD method was employed to further analyze the density and strength of surface acidic sites of pure TiO_2 and TiO_2 - WO_3 composites with 4.40 wt.% of W loading. Acidic-basic properties define behavior of catalysts in advanced oxidation processes, especially the amount and the strength of surface acidic sites [46]. Fig. 9 presents Py-TPD profiles with peaks in the low (150–400 °C) and high (450–600 °C) temperature range resulting from desorption of pyridine from weak and strong acidic sites. The profiles show that the acidic-basic properties vary significantly, depending on the TiO_2 morphology used to prepare composites. The measured density and quantity of acidic sites for the prepared samples are listed in Table 2. P-500 and P+4.40 composite contain both weak and strong acidic sites, whereas R-500 and R+4.40 composite contain only weak acidic sites. Thus, the strength of acidic sites in pure TiO_2 and TiO_2 - WO_3 composites is intrinsically determined by the morphology of the TiO_2 . Density of acidic sites, however, is independent of the catalyst morphology and measures between 0.0022 and 0.0026 mmol/m² (Table 2).

Fig. 10 is showing the diffuse reflectance FTIR spectra of both TiO_2 morphologies (nanoparticles and nanorods) and their composites with 4.40 wt.% of W at −140 °C recorded during UV irradiation (Light ON) and without UV-irradiation (Light OFF), respectively. In Fig. 10a, the presence of water molecules adsorbed

on the sample was confirmed with a characteristic peak at 1630 cm^{−1} that can be assigned to the H–O–H deformation mode. The broad and intense band between 3500 and 3000 cm^{−1} can be attributed to the surface OH stretching. As a result of the strong interaction between Ti ions and OH groups, a shoulder at 3169 cm^{−1} is observed. The broad band at around 900 cm^{−1} can be assigned to Ti–O–Ti vibration in the TiO_6 octahedra [47–49]. Illumination of TiO_2 - WO_3 composites with UV light (light ON) causes a pronounced increase in the IR absorbance over the entire region (from 4000 to 800 cm^{−1}), as shown in Fig. 10. Changes in the signal intensity are manifested as structural modifications either in the oscillating dipole moment strength and/or change in bond lengths. It is well known that the IR absorbance intensity (A) is proportional to the number (N) of conduction band electrons within the semiconductor ($A \sim N$) [50]. Szczepankiewicz et al. [20] have showed with DRIFTS measurements that during UV-illumination of TiO_2 surface, the conduction band electron can be trapped and can maintain an unusually long lifetime of minutes to hours.

Subtraction of the light OFF spectrum from the light ON spectrum produces a corrugated spectrum with three distinct sub-bands, related to spin-orbital interactions explained in detail elsewhere [51,52] (inset of Fig. 10a–d). It is known that the photogenerated electrons can be trapped in the energy states below

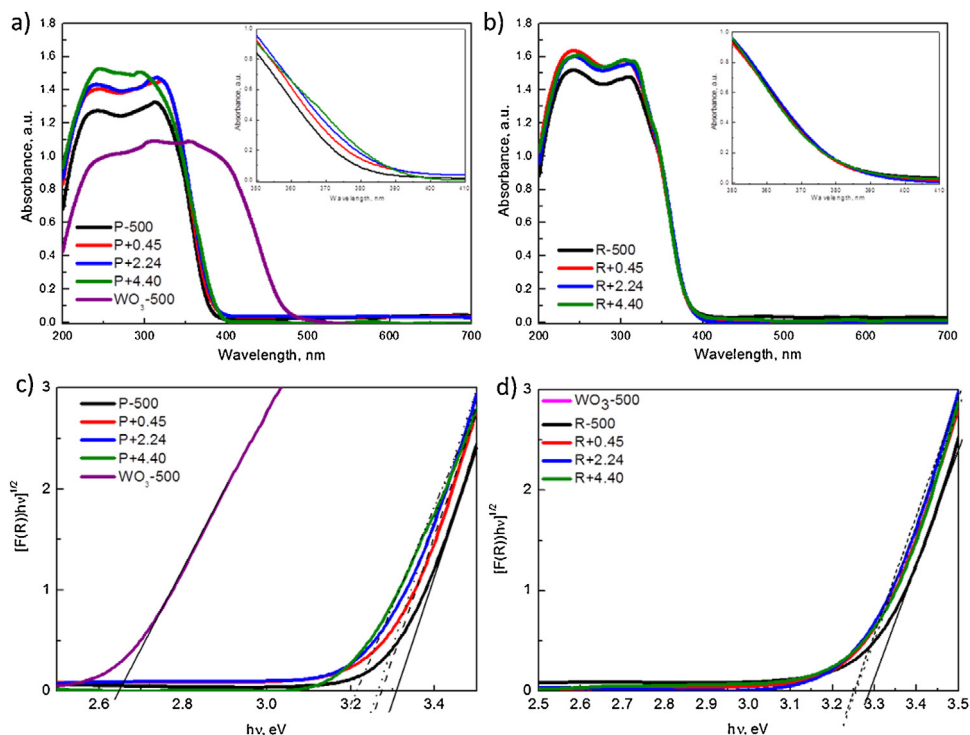


Fig. 8. UV/Vis DR spectra of (a) P-TiO₂-WO₃ and (b) R-TiO₂-WO₃ composites with different WO₃ loadings. Spectra of P-500, R-500 and WO₃-500 samples are shown for comparison. (c) and (d) present the corresponding Tauc plots applicable to TiO₂ anatase phase which possesses indirect VB→CB transition.

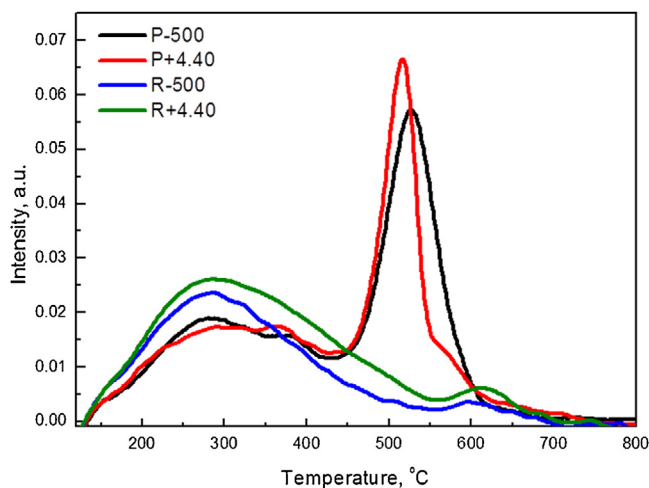


Fig. 9. Py-TPD curves for P-TiO₂-WO₃ and R-TiO₂-WO₃ composites.

CB and can cause the transient IR absorption *via* two routes: (i) the thermally excited intra CB transitions of free electrons from the trap state, and (ii) the direct optical transition from the trap state to the CB [53]. These two processes happen simultaneously and cannot be distinguished. However, at low temperatures (~ 140 °C), as used in the experiments, thermal energy is considerably low, thus thermal excitation can be ignored. Therefore, the measured IR absorption difference between light ON and light OFF experiments can be associated to their UV radiation induced transitions between the trapping states and the CB.

The intense IR absorption observed in inset of Fig. 10a (for R-500) around 1200 cm^{-1} suggests that the ionization energy of the trapping states is less than 0.15 eV which is consistent with the reported values for shallow traps (0.1 eV) [29]. Thus, in conclusion pure TiO₂ nanorods (R-500) have a high density of shallow trapping

states below the CB. Fig. 10b shows a different IR absorption intensity difference profile that probably results from different charge carrier dynamics which will be explained in next section.

Although the spectrum features are similar in inset of Fig. 10a and c, it is worth noticing that the IR absorption intensity for P-500 (Fig. 10c) is much smaller ($4\times$) than in the case of R-500 (Fig. 10a). The most plausible explanation is that the number of electrons which can be transferred to conduction band by UV illumination is much lower in P-500 sample. The energy gap between CB and trap states in the P-500 sample might be too large for trapped electrons to make IR light induced transitions; therefore no mid-IR light is absorbed. This means that the P-500 has deep trapping states (energy difference > 0.15 eV) below the CB. The possible reason for presence of deep trapping sites in this sample can be traced back to the strong surface acidic sites, which create a strong local electric field that results into the occurrence of deep trapping sites [21]. In inset of Fig. 10d, the IR absorption signal intensity is fully recovered, which reflects the improved electron mobility in the P+4.40 sample. The reason for improved charge mobility in this sample likely lies in the presence of monoclinic WO₃ phase forming a heterojunction with anatase TiO₂.

Time-resolved FTIR measurements for both TiO₂ morphologies and their composites with 4.40 wt.% of W are presented in Fig. 11. The samples were irradiation with UV-light for 28 mins (light ON) and then light was turned off for 28 min to observe the electronic decay kinetics (light OFF). Absorbance spectra were acquired every minute with and without UV irradiation. The typical temporal variation in the IR absorption during light ON and light OFF experiments for R+4.40 composite is shown in inset of Fig. 11. UV irradiation triggers rapid growth of charge carriers, which reached a plateau during the irradiation time-frame (28 min) and decay once the UV light was switched OFF, as shown in Fig. 11. The electronic decay dynamics of P-500 decreased in first few minutes and then became constant throughout the experiments. This is an indication of deep trapping states present in the sample. Strong acid sites

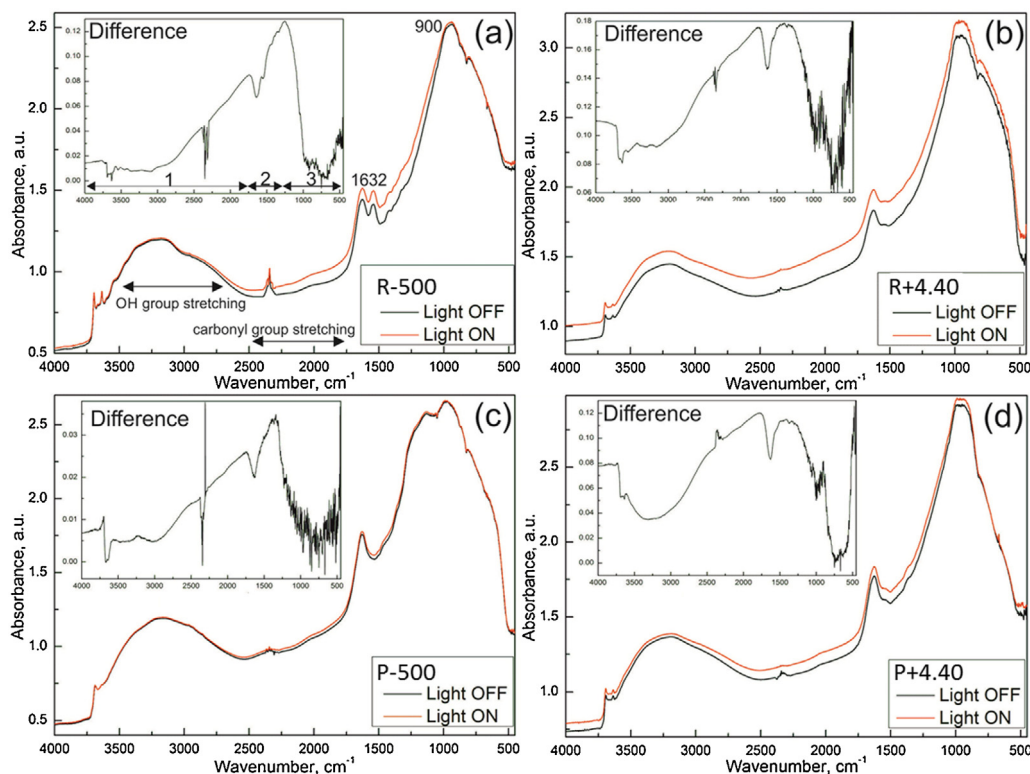


Fig. 10. *In situ* low temperature (-140°C) FTIR spectra of (a) P-500, (b) P-TiO₂-WO₃ composite with 4.40 wt.% W, (c) R-500, and (d) R-TiO₂-WO₃ composite with 4.40 wt.% W. The insets represent the difference between light ON and light OFF experiments.

were observed in this sample by the Py-TPD (Fig. 9) and pH_{PZC} measurements (see supplementary data, Fig. S3) and it is well known that surface acid sites generate a strong electric field which favors deep electron-trapping states [21]. In P+4.40 sample, the electronic decay dynamics were significantly different compared to P-500 sample, the decay profile is decreasing almost linearly with time. In this composite, monoclinic WO₃ phase is intermixed with anatase TiO₂, thus interface between the two materials exists (see TEM, Fig. 2). Under UV light irradiation of P+4.40 sample, excited electrons in TiO₂ transfer to its CB. The electrons in the CB of TiO₂ transfer further to the CB of WO₃ at the interface, as the CB edge of WO₃ is located at more positive potential than the one of TiO₂. The photo-generated holes in WO₃ valence band will transfer to TiO₂ [10,13]. The result is that the mobility of the photo-generated electrons and holes is significantly improved. For this reason, the photocatalytic efficiency of TiO₂-WO₃ composite can be improved in comparison to pure TiO₂ [11,54–56].

A rapid decay of absorption intensity was observed for R-500, which is typical for shallow trapping states as shown in Fig. 11 [33]. As observed in the previous section, the ionization energy of trapping states is around 0.15 eV in this sample, which corresponds to the energy of shallow trapping. Thus, for R-500 sample, a large density of shallow trapping states is expected. N-type semiconductor, such as anatase TiO₂ nanorods are known to possess a high density of shallow trapping states [57,58]. As a result, the photocatalytic activity of R-500 should be higher than the activity of P-500 which contains deep trapping states. For R+4.40, large electronic decay was observed, which may correspond to fast recombination. After combining TiO₂ nanorods with WO₃, the surface of TiO₂ nanorods is modified with amorphous layer of WO₃ (as evident from TEM, AFM, XRD, UV/Vis DR data), which may act as recombination centers. Indeed, relatively fast recombination is present in the case of R+4.40 sample (Fig. 11), which could subsequently reduce the photocatalytic activity of this solid. Deep trapping states are in the sense

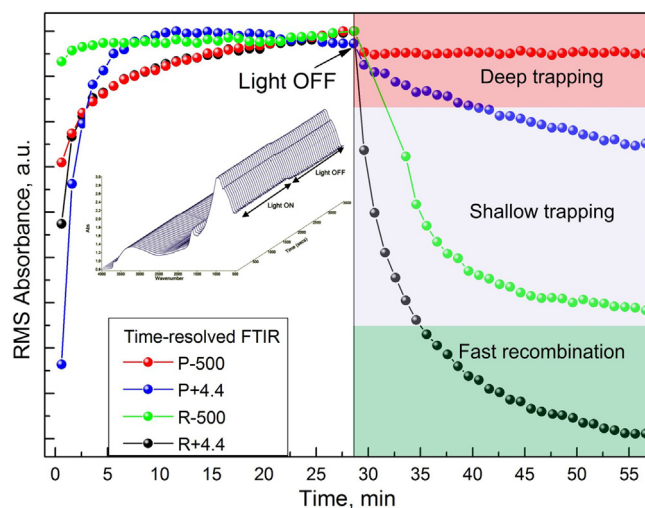


Fig. 11. Time-resolved FTIR measurement for P-TiO₂-WO₃ and R-TiO₂-WO₃ composites without and with 4.40 wt.% W. Inset is showing the typical temporal variation in the RMS absorption during light ON and light OFF experiments for R+4.40 composite.

that the energy required to remove an electron or hole from the trap to the VB or CB is much larger than the characteristic thermal energy kT , where k is the Boltzmann constant and T is temperature. This can be visualized in Fig. 11 for P-500 sample as a negligible change in RMS absorbance after the light off switch.

3.2. Photocatalytic BPA oxidation

The photocatalytic activities of TiO₂-WO₃ composites were evaluated by means of degradation of water dissolved model pollutant bisphenol A (BPA) under UVA-light irradiation. Fig. 12 shows

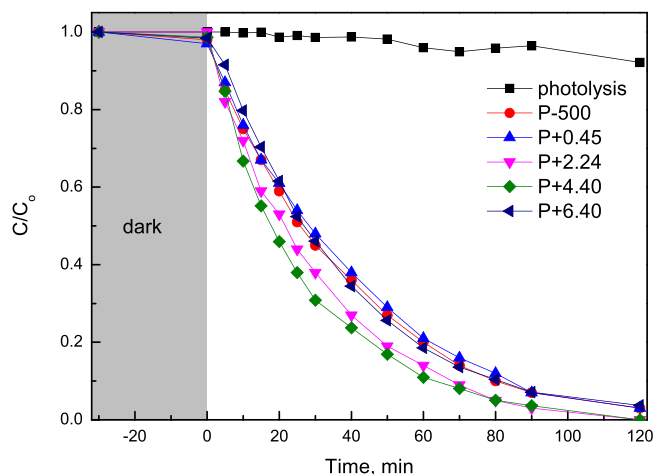


Fig. 12. Photolytic and photocatalytic degradation of BPA in the presence of P-TiO₂-WO₃ composites with different WO₃ loadings irradiated with UV light for 120 min.

Table 3

Carbon content accumulated on the surface of composite catalysts before (TC_{fresh}) and after (TC_{spent}) photocatalytic BPA degradation. TOC removal (TOC_R) combined with true TOC conversion (TOC_m).

Sample	^a TOC _R , %	TC _{fresh} , %	TC _{spent} , %	TOC _m , %
P-500	55	0.10	1.68	42.3
P+0.45	47	0.10	1.66	34.4
P+2.24	62	0.09	1.65	49.4
P+4.40	79	0.12	1.64	66.7
R-500	87	0.12	0.11	87
R+0.45	85	0.11	0.12	84.9
R+2.24	80	0.14	0.09	80
R+4.40	50	0.10	0.16	49.5

^a Reaction time: 2 h.

BPA degradation curves of P-TiO₂-WO₃ composites. The experiments were first conducted under dark conditions for 30 min in order to determinate adsorption equilibrium. The decrease of BPA concentration due to adsorption of BPA on the surface of prepared P-TiO₂-WO₃ composites was negligible and was not influenced by the amount of WO₃ present in the composites. BPA has a photo-resistant character, since the results of photolysis (no catalyst present in the reactor) show that the concentration of BPA in the solution was only slightly decreasing as a function of time under UVA illumination. The curves of BPA photocatalytic degradation in aqueous solution show that when TiO₂ nanoparticles were loaded with more than 0.45 wt.% W, the degradation of BPA was enhanced. The maximum degradation activity was achieved with the composite containing 4.40 wt.% of W. Table 3 presents the TOC removal data (TOC_R), which were obtained after 120 min of irradiation of BPA solution under UVA light in the presence of TiO₂-WO₃ composites with different amounts of WO₃ loading. The measured TOC data for TiO₂ nanoparticle composites resemble the trend of BPA degradation curves presented in Fig. 12. The extent of BPA mineralization and its reaction intermediates is not as significant as the extent of BPA removed. The TiO₂-WO₃ composites with 2.24 and 4.40 wt.% of W content enabled complete BPA removal after 120 min, but lower extent of BPA mineralization was obtained in this time span. In Table 3 are also listed the results of carbon based elemental analysis of fresh and spent composite samples. The true TOC removal (TOC_m) values consider the amount of TOC that was accumulated on the catalyst surface during the photooxidation reaction and was so only apparently removed from the irradiated BPA solution. The listed results reveal that in the case of P-TiO₂-WO₃ composites the amount of carbon on spent samples was higher than on fresh

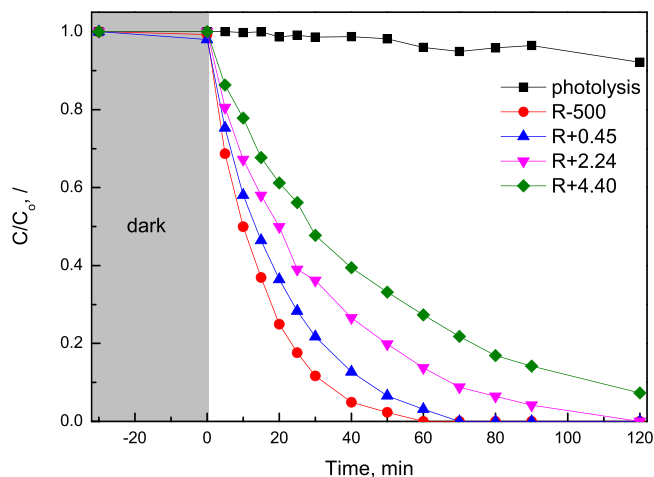


Fig. 13. Photolytic and photocatalytic degradation of BPA in the presence of R-TiO₂-WO₃ composites with different WO₃ loadings irradiated with UV light for 120 min.

solids, which is a sign that BPA or partially oxidized BPA degradation products adsorb on the catalyst surface. Nevertheless, the amount of carbon adsorbed on the surface of P-TiO₂-WO₃ composites is not influenced by the amount of WO₃ present in the composites. Comparing the TOC_m values for TiO₂ nanoparticle composites with 4.40 wt.% loading of W and P-500 reveals that the mineralization is 1.5 time more effective over the P+4.40 composite (Table 3).

With increasing the amount of WO₃ in the TiO₂ nanoparticle composites over 4.40 wt.% W the photocatalytic activity of the composite toward BPA degradation decrease (Fig. 12) and so the right amount of W in the TiO₂ nanoparticle composites is of crucial importance for the photocatalytic activity. Also other authors reported that there is an optimal amount of WO₃ in the composites and that further increase of WO₃ decreases the photocatalytic activity [10,13,55]. The reasons might be (i) excess WO₃ is not in contact with TiO₂ which is the catalytically active phase and cannot participate in the prolonging of electron-hole separation or (ii) the WO₃ fully covers the TiO₂ and hinders absorption of the UV light [13].

Fig. 13 shows temporal BPA degradation curves of R-TiO₂-WO₃ composites. As before, we can see that after 30 min of dark period, which was introduced to determine the adsorption equilibrium, the concentration of BPA in the reaction suspension did not change significantly due to adsorption of BPA onto the surface of examined catalysts. BPA degradation curves presented in Fig. 13 demonstrate that already small amount (0.45 wt.%) of WO₃ introduced into R-TiO₂-WO₃ composites decrease the photocatalytic activity of composites, compared to R-500. The observed decrease of the photocatalytic activity is almost linear with the increase of WO₃ loading in the composite. The results of TOC measurements listed in Table 3 show the same trend, since the extent of mineralization decreases with increasing WO₃ loading in the R-TiO₂-WO₃ composites. Carbon elemental analysis of fresh (TOC_{fresh}) and spent (TOC_{spent}) R-TiO₂-WO₃ composites shows that in contrast to P-TiO₂-WO₃ composites, accumulation of carbon onto the surface of TiO₂ nanorod based composites during BPA degradation is negligible in the given range of operating and reaction conditions. Based on the presented results, it can be concluded that the enhanced accumulation of carbon-containing species on the surface of TiO₂ nanoparticle composites during the degradation of BPA is attributed to the presence of strong acidic sites, as determined by Py-TPD analysis (Fig. 9, Table 2).

The results of BPA degradation runs (Figs. 12 and 13) show that the composite P+4.40 and R-500 exhibit enhanced photocatalytic

activity in comparison to P-500 and R+4.40 solids, respectively. This can be explained by taking into account the results of time-resolved FTIR measurements (Fig. 11). It was discovered that in the case of P+4.40 and R-500 samples shallow trapping of excited electrons occurs, which favors photocatalytic activity of catalysts. On the other hand, the photocatalytic activities of R+4.40 and P-500 materials are deteriorated because in the first case recombination of electrons with VB holes is too fast, while in the second case (P-500) traps are too deep from the CB, which consequently reduces the photocatalytic activity. In case of P-TiO₂-WO₃ composites, BPA degradation curves show that a heterojunction between WO₃ and TiO₂ is formed which hinders the electron-hole recombination rate by trapping the electrons as was already observed by other authors when combining TiO₂ and WO₃ [10–13], and so the photocatalytic activity of the composites is improved in comparison to P-500. R-500 sample have high density of shallow trapping sites, which favors photocatalytic activity of catalyst. On the other hand, the photocatalytic activities of R-TiO₂-WO₃ composites with increasing amount of WO₃ are deteriorated because of the amorphous layer form on the surface of the TiO₂ nanorods which acts as a recombination centers for photoelectrons.

4. Conclusions

The results of TEM, UV/Vis DR, XRD, and AFM measurements have shown that when TiO₂ NRs and WO₃ are combined by means of incipient wet impregnation procedure, WO₃ is dispersed over the surface of TiO₂ NRs in the amorphous form. With increasing amount of WO₃ in R-TiO₂-WO₃ composites, the extent of surface coverage with amorphous WO₃ increases. On the contrary, in the case of composites comprising TiO₂ polyhedral nanoparticles (P-TiO₂-WO₃), crystalline monoclinic WO₃ is intermixed with anatase TiO₂.

Time-resolved FTIR measurements revealed that in the R-500 and P+4.40 solids shallow trapping sites are predominantly present. On the other hand, deep trapping or fast electron-hole recombination appear in P-500 and R+4.40 samples, respectively. The structural differences in WO₃ result in different electronic structure and energy levels, which in turn present intrinsically different trapping states for charge carriers. As a result, addition of WO₃ improves photocatalytic activity in P-500 based materials and deteriorates it in R-500, which was confirmed by photocatalytic BPA degradation experiments.

The results of photocatalytic BPA degradation show that in the case of P-TiO₂-WO₃ composites, the overall photocatalytic activity increases with rising WO₃ content and reaches a maximum with 4.40 wt.% of W loading before it start to decrease. On the other hand, for R-TiO₂-WO₃ composites, the photocatalytic activity continuously decreases with increasing amount of WO₃. This can be explained by taking into account the results of TEM, Py-TPD and time-resolved FTIR measurements, which indicate that in the case of P-500 catalyst, deep electron traps are present due to the strong acid sites, which hinder the electronic mobility and consequently reduce the photocatalytic activity. Introduction of WO₃ into the P-TiO₂-WO₃ composites facilitated the transition of electrons from the CB of TiO₂ to CB of WO₃ and simultaneous migration of photo-generated holes from the valence band of WO₃ to the valence band of TiO₂. The result is significantly improved charge carrier separation which led to higher photocatalytic activity.

R-500 catalyst was found to contain a high density of shallow trapping sites, which favor photocatalytic activity. The photocatalytic activity of R-TiO₂-WO₃ composites deteriorates with increasing amount of WO₃ because this amorphous layer on the surface of the TiO₂ nanorods provides recombination centers for photoelectrons. It was discovered that shallow trapping

of electrons is important to increase the photocatalytic activity of TiO₂-WO₃ catalysts and besides the rate of electron-hole recombination, the energy levels of trapping states should be considered when tailoring such composite photocatalysts.

Acknowledgements

The authors gratefully acknowledge the financial support of the Ministry of Education, Science and Sport of the Republic of Slovenia through Research program No. P2-0150.

Appendix A. Supplementary data

Supplementary data associated with this article can be found, in the online version, at <http://dx.doi.org/10.1016/j.apcatb.2017.02.059>.

References

- [1] P. Chen, K.G. Linden, D.E. Hinton, S. Kashiwada, E.J. Resenfeldt, S.W. Kullman, *Chemosphere* 65 (2006) 1094–1102.
- [2] J.L. Wang, L.J. Xu, *Crit. Rev. Environ. Sci. Technol.* 42 (2012) 251–325.
- [3] K. Hashimoto, H. Irie, A. Fujishima, *Jpn. J. Appl. Phys.* 12 (2005) 8269–8285.
- [4] J. Zhang, Q. Xu, Z. Feng, M. Li, C. Li, *Angew. Chem.* 9 (2008) 1766–1769.
- [5] G.K. Mor, H.E. Prakasam, O.K. Varghese, K. Shanker, C.A. Grimes, *Nano Lett.* 7 (2007) 2356–2364.
- [6] Z. Jiang, F. Yang, N.J. Luo, B.T.T. Chu, D. Sun, H.H. Shi, T.C. Xiao, P. Edwards, *Chem. Commun.* 47 (2008) 6372–6374.
- [7] R. Asahi, T. Morikawa, T. Ohwaki, K. Aoki, Y. Taga, *Science* 293 (2001) 269–271.
- [8] C. Wang, J.C. Zhao, X. Wang, B.X. Mai, G.Y. Sheng, P.A. Peng, J.M. Fu, *Appl. Catal. B-Environ.* 39 (2002) 269–279.
- [9] S. Anandan, M. Yoon, *J. Photochem. Photobiol. C: Rev.* 4 (2003) 5–18.
- [10] S.A. Singh, G. Madras, *Sep. Purif. Technol.* 105 (2013) 79–89.
- [11] H. Song, H. Jiang, X. Liu, G. Meng, *J. Photochem. Photobiol. A* 181 (2006) 421–428.
- [12] S. Anandan, T. Sivasankar, T. Lana-Villarreal, *Ultrason. Sonochem.* 21 (2014) 1964–1968.
- [13] B.J. Ma, J. Kim, T. Wang, J. Li, K.Y. Lin, W.Y. Liu, S. Woo, *RSC Adv.* 97 (2015) 79815–79819.
- [14] H. Yang, R. Shi, K. Zhang, Y. Hu, A. Tang, X. Li, *J. Alloys Compd.* 398 (2005) 200–202.
- [15] C. Shifu, C. Lei, G. Shen, C. Gengyu, *Powder Technol.* 106 (2005) 198–202.
- [16] J. Engewiler, J. Harf, A. Baiker, *J. Catal.* 1599 (1996) 259–269.
- [17] A. Ulgen, W.F. Hoelderich, *Appl. Catal. A-Gen.* 400 (2011) 34–38.
- [18] K.K. Akurati, A. Vital, J.-P. Dellemann, K. Michalow, T. Graule, D. Ferri, A. Baiker, *Appl. Catal. B-Environ.* 79 (2008) 53–62.
- [19] B. Ohtani, *Catalysts* 3 (2013) 942–953.
- [20] S.H. Szczepankiewicz, J.A. Moss, M.R. Hoffmann, *J. Phys. Chem. B* 106 (2002) 2922–2927.
- [21] S.H. Szczepankiewicz, J.A. Moss, M.R. Hoffmann, *J. Phys. Chem. B* 106 (2002) 7654–7658.
- [22] H. Böttger, V.V. Bryksin, *Phys. Stat. Solid B* 78 (1976) 9–56.
- [23] Z. Jiang, L. Kong, F. Sh. Alenazey, Y. Qian, L. France, T. Xiao, P.P. Edwards, *Nanoscale* 5 (2013) 5396–5402.
- [24] N. Murakami, R. Abe, B. Ohtani, *Chem. Phys. Lett.* 416 (2008) 316–320.
- [25] D.P. Colombo, R.M. Bowman, *J. Phys. Chem.* 100 (1996) 18445–18449.
- [26] M. Styliadi, D.I. Kondarides, X.E. Verykios, *Appl. Catal. B-Environ.* 40 (2003) 271–286.
- [27] J.M. Coronado, A.J. Maira, J.C. Conesa, K.L. Yeung, V. Augugliaro, J. Soria, *Langmuir* 17 (2001) 5368–5374.
- [28] A. Emeline, A. Salinaro, N. Serpone, *J. Phys. Chem. B* 104 (2000) 11202–11210.
- [29] T. Berger, M. Sterrer, O. Diwald, E. Knöziger, *J. Phys. Chem. B* 109 (2005) 6061–6068.
- [30] D.W. Bahnemann, M. Hilgendorff, R. Memming, *J. Phys. Chem. B* 101 (1997) 4265–4275.
- [31] H. Kukimoto, S. Shionoya, T. Koda, R. Hioki, *J. Phys. Chem. Solids* 29 (1968) 935–944.
- [32] H. Kukimoto, R. Hioki, T. Koda, S. Shionoya, *Phys. Lett.* 19 (1965) 551–552.
- [33] D.M. Savory, A.J. McQuillan, *J. Phys. Chem. C* 117 (2013) 23645–23656.
- [34] T. Kasuga, M. Hiramatsu, A. Hoson, T. Sekino, K. Niihara, *Adv. Mater.* 11 (1999) 1307–1311.
- [35] C.J. Howard, T.M. Sabine, F. Dickson, *Acta Cryst. B* 47 (1991) 462–468.
- [36] B. Erjavec, T. Tišler, R. Kaplan, A. Pintar, *Ind. Eng. Chem. Res.* 52 (2013) 12559–12566.
- [37] M. Bledowski, L. Wang, A. Ramakrishnan, O.V. Khavryuchenko, V.D. Khavryuchenko, P.C. Ricci, J. Strunk, T. Cremer, C. Kolbeck, R. Beranek, *Phys. Chem. Chem. Phys.* 13 (2011) 21511–21519.
- [38] M.A. Saepurahman, F.K. Abdullah, Chong, J. Hazard. Mater. 176 (2010) 451–458.
- [39] Y. Yamin, N. Keller, V. Keller, *J. Photochem. Photobiol. A* 245 (2012) 43–57.

- [40] C.W. Lai, S. Sreekantan, W. Krengvirat, E. Pei San, *Electrochem. Acta* 77 (2012) 128–136.
- [41] W.H. Lee, C.W. Lai, S. Bee Abd Hamid, *Materials* 8 (2015) 2139–2153.
- [42] J. Zhu, S. Wang, S. Xie, H. Li, *Chem. Commun.* 47 (2011) 4403–4405.
- [43] C. Martin, G. Solana, V. Rives, *Catal. Lett.* 49 (1997) 235–243.
- [44] A. Gutierrez-Alejandre, J. Ramirez, G. Busca, *Catal. Lett.* 56 (1998) 29–33.
- [45] P. Basnet, Y. Zhao, *J. Mater. Chem.* 2 (2014) 911–914.
- [46] S. Prabhu, A. Nithya, S. Chandra Mohan, K. Jothivenkathachalam, *Mater. Sci. Forum* 781 (2014) 63–78.
- [47] W. Wang, J. Zhang, H. Huang, Z. Wu, Z. Zhang, *Colloid. Surf. A* 317 (2008) 270–276.
- [48] L. Qian, Z.S. Jin, S.Y. Yang, Z.L. Du, X.R. Xu, *Chem. Mater.* 17 (2005) 5334–5338.
- [49] M.L. Qian, T. Zhang, S. Wageh, Z.S. Jin, Z.L. Du, Y.S. Wang, X.R. Xu, *Nanotechnology* 17 (2006) 100–104.
- [50] N. Siedl, P. Gügel, O. Diwald, *J. Phys. Chem. C* 2013 (2013) 20722–20729.
- [51] R.G. Breckenridge, W.R. Hosler, *Phys. Rev.* 91 (1953) 793–802.
- [52] A.L. Linsebigler, G. Lu, J.T. Yates, *Chem. Rev.* 95 (1995) 735–758.
- [53] A. Yamakata, T.-A. Ishibashi, H. Onishi, *Chem. Phys. Lett.* 333 (2001) 271–277.
- [54] A. Benoit, I. Paramasivam, Y.-C. Nah, P. Roy, P. Schmuki, *Electrochem. Commun.* 1 (2009) 728–732.
- [55] H. Sun, B. Dong, G. Su, R. Gao, W. Liu, L. Song, L. Cao, *Appl. Surf. Sci.* 343 (2015) 181–187.
- [56] G.R. Bamwenda, H. Arakawa, *Appl. Catal. A-Gen.* 210 (2001) 181–191.
- [57] X. Chen, S.S. Mao, *Chem. Rev.* 107 (2007) 2891–2959.
- [58] M.A. Henderson, *Surf. Sci. Rep.* 66 (2011) 185–297.